CrossMark

RESEARCH ARTICLE

Sound source localization on an axial fan at different operating points

Florian J. Zenger[1] · Gert Herold[2] · Stefan Becker[1] · Ennes Sarradj[2]

Abstract A generic fan with unskewed fan blades is investigated using a microphone array method. The relative motion of the fan with respect to the stationary microphone array is compensated by interpolating the microphone data to a virtual rotating array with the same rotational speed as the fan. Hence, beamforming algorithms with deconvolution, in this case CLEAN-SC, could be applied. Sound maps and integrated spectra of sub-components are evaluated for five operating points. At selected frequency bands, the presented method yields sound maps featuring a clear circular source pattern corresponding to the nine fan blades. Depending on the adjusted operating point, sound sources are located on the leading or trailing edges of the fan blades. Integrated spectra show that in most cases leading edge noise is dominant for the low-frequency part and trailing edge noise for the high-frequency part. The shift from leading to trailing edge noise is strongly dependent on the operating point and frequency range considered.

1 Introduction

A lot of effort has been devoted to the optimization of axial fans. In addition to efficiency and aerodynamics, such optimization strategies are increasingly focused on the reduction in aeroacoustic noise emission (Kim et al. 2014; Bamberger and Carolus 2012). In order to develop effective measures for lower sound emission, a thorough knowledge of the sound generation in axial fans is necessary. This includes the frequency-dependent location and strength of sound sources at various operating points.

Microphone array methods, such as beamforming, are widely used for characterizing aeroacoustic noise sources. In this process, the phase shifts from discretized focus points to microphone positions are evaluated, yielding a sound map. A distinction is drawn between algorithms in the time and frequency domains. In the time domain, the signals are shifted in accordance with the sound propagation from the focus point to the microphone. Subsequently, the signals are summed, resulting in the sound pressure for the considered focus point (Underbrink 2012). In the frequency domain, the signals are Fourier transformed block-wise and their cross-spectra are averaged to obtain the cross-spectral matrix (CSM). The CSM is then multiplied by steering vectors, containing the sound propagation model from focus points to the microphones (Underbrink 2012). Using frequency-domain beamforming, deconvolution methods can be applied to increase the dynamic range and resolution of the resulting sound map.

Microphone array methods cannot be applied directly to rotating objects, as the relative motion of the sound source to the microphone array needs to be considered. Sijtsma et al. (2001) approached this challenge by using a transfer function for a moving monopole to reconstruct the source signal in the time domain. The algorithm was validated with rotating whistles and applied to localize sound sources on helicopter and wind turbine blades (Sijtsma et al. 2001) and also on a turbofan engine (Sijtsma 2010).

✉ Florian J. Zenger
ze@ipat.uni-erlangen.de

Gert Herold
herold@b-tu.de

[1] Institute of Process Machinery and Systems Engineering, Friedrich-Alexander University Erlangen-Nürnberg, Cauerstr. 4, 91058 Erlangen, Germany

[2] Chair of Technical Acoustics, Brandenburg University of Technology, Siemens-Halske-Ring 14, 03046 Cottbus, Germany

Benedek and Tóth (2013) employed this method for localizing sound sources on a ducted fan. They observed different source spots in the rotating frame, but were not able to detect distinct circular source patterns corresponding to the fan blades. Benedek and Vad (2014) investigated a forward-skewed fan, installed in a short duct, with the same method. In the 4 kHz third-octave band and at lower frequencies, dominant noise sources were found in the mid-span region, resulting from a locally thickened suction-side boundary layer. At higher frequencies, the sound levels of the electric motor in the hub were comparable to the sound sources on the fan blades. In the blade region, the main sound sources were found near the blade tip, hinting at tip leakage-related phenomena.

Minck et al. (2012) used a similar method to analyze a ducted fan with eleven fan blades. Sound maps were evaluated from measurements with and without obstacles on two fan blades, forcing flow detachment on those blades. With obstacles on the blade, dominant noise sources on the leading edge of the following blades in the tip region could be detected. Without obstacles, sound sources on the leading edges of the fan blades were observed at each fan blade for a frequency of 5 kHz.

The above investigations all involved time-domain applications of microphone array methods for rotating sources. In addition, there also exist approaches that use frequency-domain beamforming methods. These methods rely on motion compensation of the rotating fan.

Lowis and Joseph (2006) used Green's function for a rotating monopole to determine the strength of rotating sources in the rotating frame of a ducted fan. Pannert and Maier (2014) similarly used Green's function of a rotating monopole under free-field conditions to reconstruct the CSM for a virtual rotating array from the CSM calculated from a stationary array. Beamforming algorithms with deconvolution were then used for evaluating simulated signals and measurements with rotating piezo speakers. Sound maps showed a significant improvement in terms of dynamic range and resolution compared with beamforming algorithms without deconvolution. However, using Green's function to reconstruct microphone signals or CSM is only feasible if the rotation of the investigated object is uniform and with a constant rotational frequency. In experimental investigations, this requirement is not always fulfilled.

Dougherty and Walker (2009) took a different approach in dealing with the relative rotation for in-duct beamforming on a fan. In the special case of a circular movement, the rotational symmetry can be taken advantage of, if the array microphones are arranged on a ring, coaxial to the rotational axis of the sound source. One or more rings of microphones were arranged up- and downstream of the investigated fan. The microphone data were resampled after acquisition to a rotating frame with the same rotational speed as the fan by interpolation of the microphone signals. This enabled the use of beamforming algorithms in the frequency domain with deconvolution. Distinct source patterns could be observed for various frequencies.

Herold and Sarradj (2015) adapted this method, taking into account a non-constant rotational fan speed. The interpolation to a virtual rotating array is not bound to a constant rotational speed and therefore can also be applied to objects with varying rotational movement. For the case of a low-speed axial fan, it was shown that sound sources can mainly be found at the trailing edges for higher frequencies. The same method was applied by Herold and Sarradj (2016) to investigate sources occurring on an in-duct fan with a wall-mounted array inside the duct.

There is a high potential benefit of using microphone array methods for sound source localization on rotating systems. The aim of this work is to make use of these advanced techniques for the acoustic characterization of a generic low-speed axial fan. The focus is on sound source localization and integrated spectra of sub-components at five different operating points along the fan characteristic curve. The experiments conducted for this study are intended to be part of a database created for the validation of aeroacoustic simulations, in particular numerical calculations of acoustic source terms.

2 Theory

The data processing follows the approach described by Herold and Sarradj (2015). For this, the sound pressures have to be measured at sensors positioned on a circular array, which is centered and aligned with the axis of rotation of the fan.

The first step is to transform the measured time data from the stationary system into a reference system rotating synchronously with the fan. Since the beamforming method requires the sources of interest to be non-moving, using the average rotational speed is often not sufficient in practice. Therefore, the rotational movement of the fan is tracked revolution by revolution. From that, the real-time angular position of the fan is calculated. The virtual rotating data are then calculated by linearly interpolating the measured sound pressures between two neighboring microphones according to the calculated angles.

The data are transformed into the frequency domain using Welch's method: The signal is divided into overlapping blocks of 2048 samples each, onto which a fast Fourier transform (FFT) is applied. The resulting complex sound pressures p are cross-correlated, and the cross-spectral matrix is approximated by averaging the cross-spectra:

$$C = \overline{pp^{\mathrm{H}}}. \tag{1}$$

With the basic delay-and-sum beamformer formulation in frequency domain:

$$b(\boldsymbol{x}_t) = \boldsymbol{h}^{\mathrm{H}}(\boldsymbol{x}_t) \, \boldsymbol{C} \, \boldsymbol{h}(\boldsymbol{x}_t), \quad t = 1 \ldots N, \tag{2}$$

spatial filtering of the sound pressure caused at the array center is realized, where $b(\boldsymbol{x}_t)$ describes the portion originating from one of N focus points $\boldsymbol{x}_t$. The steering vector $\boldsymbol{h}$ contains the sound propagation model. It has as many entries as microphones used (M) and "steers" the array to a chosen focus point. Assuming a monopole sound propagation model, its entries can be calculated via

$$h_m = \frac{1}{r_{t,0} r_{t,m} \sum_{l=1}^{M} r_{t,l}^{-2}} \, \mathrm{e}^{-jk(r_{t,m}-r_{t,0})}, \quad m = 1 \ldots M. \tag{3}$$

Sarradj (2012) showed that known steering vector formulations always make a small error in the calculation of either the source positions or pressure amplitudes. The formulation used in Eq. (3) ensures the correct reconstruction of the pressure amplitudes while allowing a small positional error.

The result obtained by evaluating Eq. (2) on a grid of focus points can be regarded as the actual source level distribution being convoluted with an a priori unknown point spread function (PSF). This PSF depends on the array geometry, the focus grid and the source characteristics. Several deconvolution algorithms, which enhance the spatial resolution of the beamformer map, have been proposed. In addition to being a fast method, the CLEAN-SC algorithm, as introduced by Sijtsma (2007), has the advantage of not requiring a known PSF. Instead, the PSF is estimated by identifying correlated portions of the beamformer output. For the deconvoluted result, only the maxima of the correlated portions are taken into account.

The display of reconstructed sound pressure levels on a chosen focus grid is commonly referred to as a sound map and is the basis for further investigations. Important data acquisition and processing parameters in this investigation are listed in Table 1.

3 Experimental setup

All investigations were performed on a generic fan with unskewed fan blades, designed and manufactured at the University of Erlangen-Nuremberg. The basic design parameters are listed in Table 2.

The total-to-static pressure coefficient ψ_{ts} and flow rate coefficient Φ are defined as

$$\Phi = \frac{4\dot{V}}{\pi^2 D^3 n} \tag{4}$$

$$\psi_{\mathrm{ts}} = \frac{2\Delta p_{\mathrm{ts}}}{\rho(D\pi n)^2}. \tag{5}$$

Table 1 Data acquisition and processing parameters

Parameter	Value
Number of microphones	64 + 1
Diameter of ring array	1 m
Distance from fan to array	0.45 m
Measurement time	30 s
Sampling rate	48 kHz
FFT block size	2048 samples
FFT window	von Hann
	50 % overlap
Resolution of focus grid	0.01 m
CLEAN-SC iterations	500
CLEAN-SC damping	0.6

Table 2 Fan design parameters

Design parameter	Value
Rotor diameter D	0.495 m
Hub diameter D_{hub}	0.248 m
Number of blades z	9
Rotational speed n	24.8 s^{-1}
Flow rate coefficient Φ	0.18
Total-to-static pressure coefficient ψ_{ts}	0.18

where $\dot{V}$ is the volumetric flow, Δp_{ts} is the total-to-static pressure difference and ρ is the air density. The fan was installed in a short duct with an inlet bellmouth on the suction side and a diffusor on the pressure side (see Fig. 1). The fan was driven by an external motor outside the duct. The angular position of the fan was determined with an optical fork sensor (one 3 V pulse per revolution), which was installed on the torque meter and acquired synchronously to the microphone data.
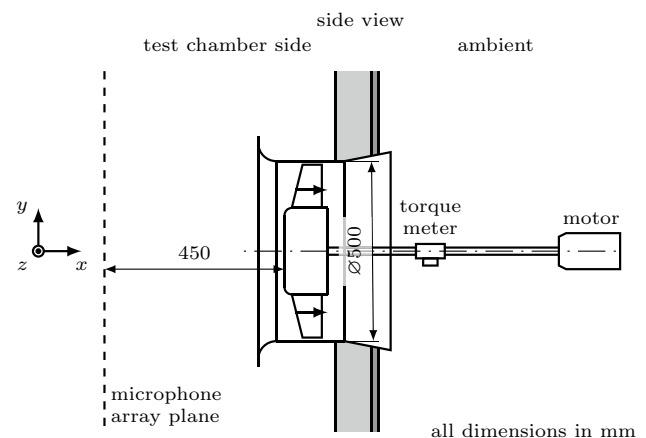

Fig. 1 Measurement setup: fan installation and microphone array position
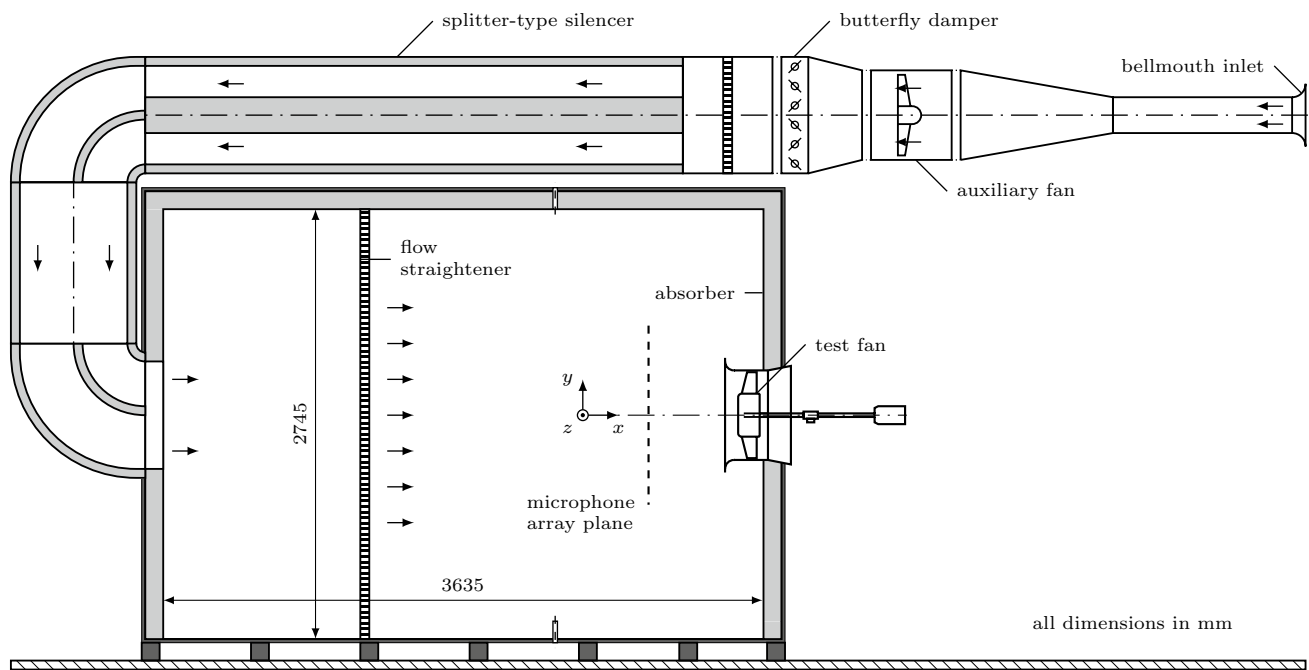
Fig. 2 Standardized inlet test chamber according to ISO 5801

The test setup was integrated in a standardized inlet test chamber according to ISO 5801 (ISO 2007), as shown in Fig. 2. The test chamber was equipped with absorbing walls and ceiling, providing semi-free-field conditions. The fan's operating point, in particular the flow rate coefficient, was carefully adjusted on every measurement point.

The microphone array consisted of 65 microphones, type 40PH-Sx (G.R.A.S. Sound and Vibration A/S). One microphone was placed on the rotational axis of the fan with a distance of 550 mm to the fan (Fig. 3). The remaining 64 microphones were arranged equidistant on a circle with a diameter of 1 m and a distance of 450 mm to the fan (see Fig. 1).

For data acquisition, a PXIe-1075 front end with PXIe-4496 data acquisition modules (National Instruments Corporation) were used. Microphone data and signals from the optical fork sensor were acquired simultaneously with a sampling frequency of 48 kHz for 30 s.

4 Results

The following sections give an overview of the fan aerodynamic and acoustic characteristic curve, sound maps and integrated spectra.

4.1 Fan characteristic curve

The aerodynamic and acoustic characteristic curves are shown in Fig. 4.

Fig. 3 Generic test fan (rotational direction: clockwise) and microphone array

The overall sound power level L_W was calculated from previous measurements, with a measurement setup as described by Zenger et al. (2015). Microphone array measurements were made at five points along the characteristic curve, marked with arrows in Fig. 4. At the operating point with the highest flow rate coefficient of $\Phi = 0.22$, the fan blades are moderately loaded, resulting in the lowest observed sound power level of $L_W = 78.3$ dB. At the design point of $\Phi = 0.18$, the blades are highly loaded and the fan is operating close to its maximum achievable pressure rise without stall (at $\Phi = 0.155$). Thus, the sound power level increases to $L_W = 87.8$ dB. At $\Phi = 0.14$, the fan is
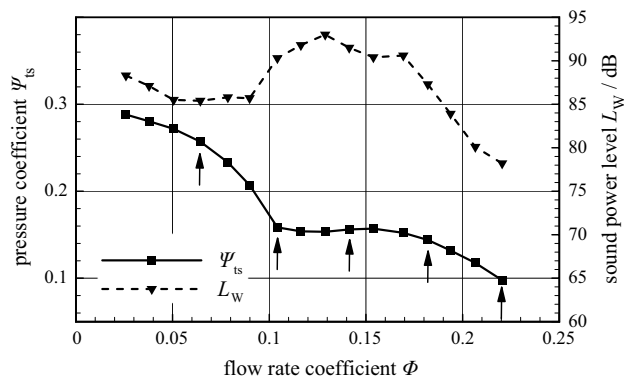
Fig. 4 Aerodynamic and acoustic characteristic curve

Fig. 5 Sound power spectra at different operating points

operating shortly after stall onset, with $L_W = 91.7$ dB. At $\Phi = 0.105$ and $\Phi = 0.065$, the fan is operating in the deep-stall region. However, as the volumetric flow decreases, so does the overall sound power level, with $L_W = 90.4$ dB ($\Phi = 0.105$) and $L_W = 85.4$ dB ($\Phi = 0.065$).

4.2 Sound power spectra

Sound power spectra serve as an overview of the evaluated frequency bands with the virtual rotating microphone array. Spectra at the five operating points are shown in Fig. 5.

At high flow rate coefficients of $\Phi = 0.18$ and 0.22, tonal and broadband components can be observed. Tonal components at the blade passing frequency (BPF) at $f_{BPF} = 225$ Hz and harmonics result from steady and unsteady loading noise, broadband components from turbulence ingestion noise and fan blade self-noise. When the fan is operated at and beyond the stall region of $\Phi < 0.155$, tonal components disappear as broadband noise, caused by the detached flow on the fan blades, becomes more dominant.

4.3 Sound maps

A three-dimensional focus grid is defined to encompass fully the area of the fan, with $r_{min} = 0.1$ m, $r_{max} = 0.35$ m and a total length in the x-direction of $l_x = 0.1$ m. The resolution of focus points is set to be 0.01 m parallel to the plane of the array and 0.02 m in the axis direction. The center part in the focus grid was omitted in this investigation as to eliminate artificial sources near the rotational axis that can occur due to small alignment discrepancies and the resulting interpolation errors. A view of one of the six grid planes in axis direction is displayed in Fig. 6. The results calculated on the three-dimensional focus region are summed in the x-direction to obtain a two-dimensional sound map.
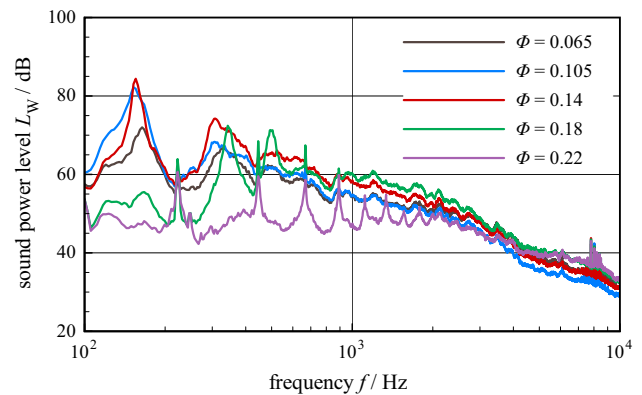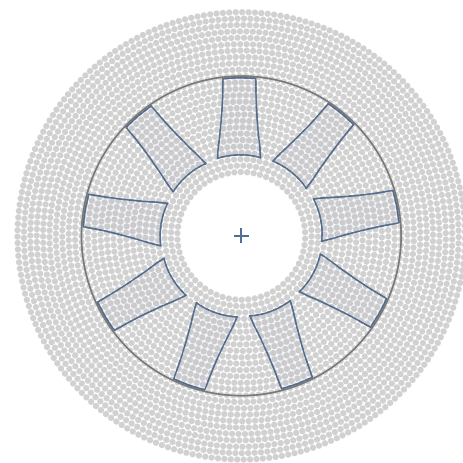

Fig. 6 View in axis direction of one focus grid plane

Sound maps are evaluated for third-octave bands with center frequencies 1, 2, 5, 8 kHz and for five different flow rate coefficients (see Fig. 7). The dynamic range of 20 dB for each map is adapted according to the maximum value in the specific map as the upper limit. A common dynamic range for each third-octave band was not beneficial in this case, as there are differences of up to 8 dB in the maximum values for the five flow rate coefficients.

4.3.1 1 kHz third-octave band

In the 1 kHz third-octave band, no clear repetitive pattern of sound sources, corresponding to the nine fan blades, can be observed. This demonstrates the limitation in resolving sound sources at low frequencies. Dougherty et al. (2013) specified the minimum resolvable distance of two point sources of equal strength by employing the Sparrow limit:
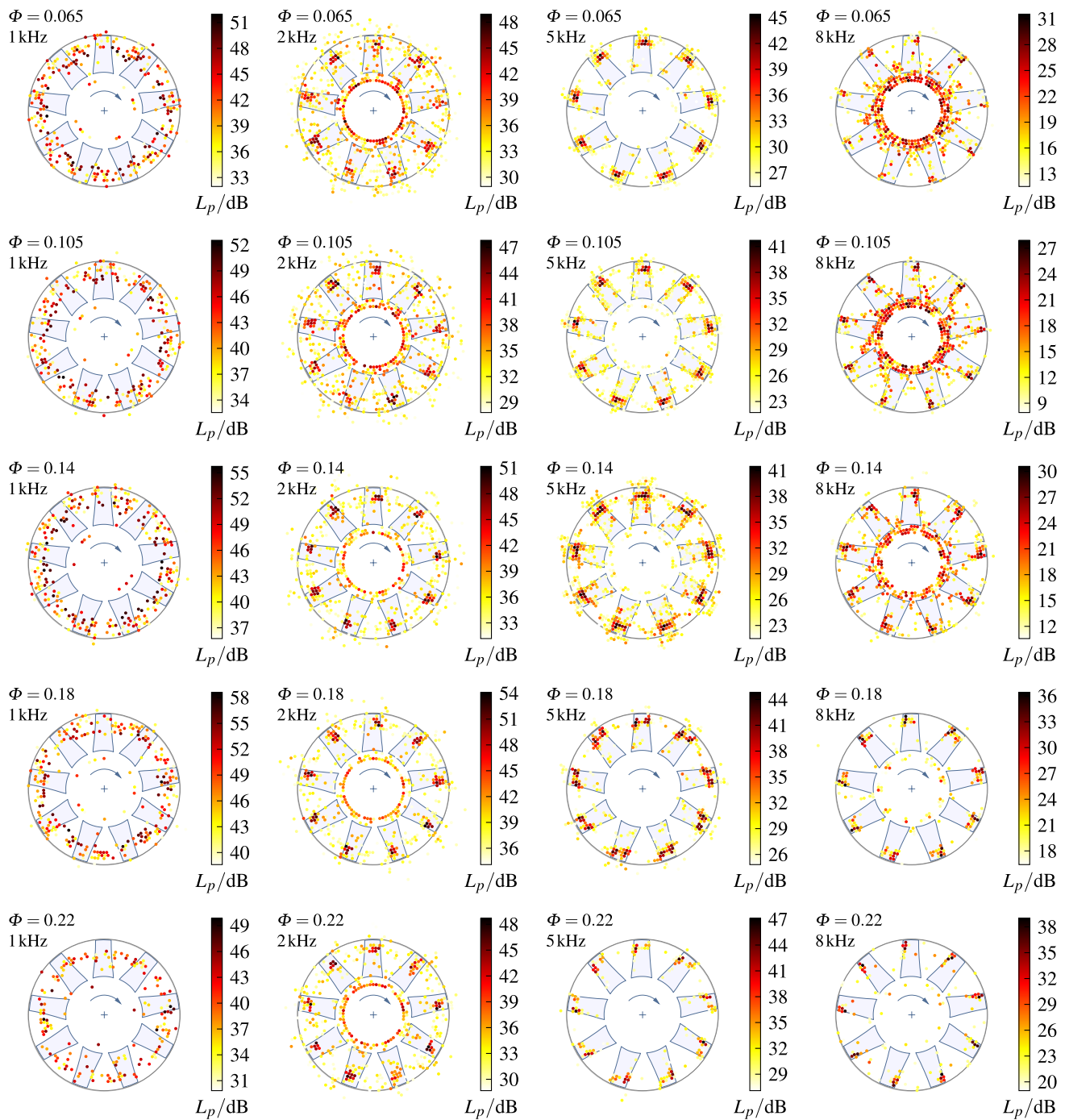
Fig. 7 Sound maps for different flow rate coefficients and third-octave bands

$$r_{\mathrm{min,CLEAN\text{-}SC}} = 0.96 \cdot 0.47 \cdot \frac{\lambda}{\sin\theta}, \qquad (6)$$

where θ is the half-angle under which the array aperture is seen from a focus point. In the case at hand, this calculates to approximately 0.2 m for 1 kHz, which exceeds even the distances of the blade tips.

Sources are mostly located in the upper half of the fan blade and in the tip region. As the angular velocity and therewith the relative flow velocity increase from the fan hub toward the blade tip, aeroacoustic sound sources are expected to be found in this region. However, no clear statement of the exact location on the fan blade can be given in this frequency range.

4.3.2 2 kHz third-octave band

Sound sources for all flow rate coefficients are mainly distributed at the outer hub, the fan blade leading edges and the blade surfaces. Only a few sound sources are located outside the fan region. Possible reasons for those physically unlikely source locations are reflections inside the duct, which have not been taken into account in the sound propagation model, or disturbances of the sound propagation caused by the flow.

Sources on the fan hub occur due to the interaction of the flow with the hub during the directional change, due to flow separations on the rounded edge of the hub, as shown in Fig. 3, or due to reflections on the reverberant aluminum hub. These sources are independent of the angular position of the fan and feature similar characteristics in terms of strength and extent for all five flow rate coefficients.

A clear repetitive pattern, corresponding to the nine blades, can be seen in the fan region. Sound sources are located in the upper third on the blade leading edge for flow rate coefficients $\Phi \in [0.065, 0.18]$.

For $\Phi < 0.18$, the fan is operating in the stall region; hence, sound sources are generated by flow separations near the leading edge.

At the design point of $\Phi = 0.18$, sound sources occur due to the interaction of the fan blade leading edge with the inflow (Blake 1986; Chou 1990). As there is a higher angular velocity at greater radii, the interaction of the inflow with the blade leading edges occurs at a higher relative velocity for greater radii. This results in a higher source strength near the blade tip.

For $\Phi = 0.22$, the fan blades are only moderately loaded. In this case, sound sources are shifted from the leading edge to the fan blade surface. These sources can be induced by the turbulent boundary layer on the fan blade suction side (Blake 1986; Wright 1976).

The maximum values in each map increase with rising volumetric flow until $\Phi = 0.18$, with a maximum of $L_p = 54$ dB at the design flow rate coefficient. This trend can also be observed in the overall sound power spectra shown in Fig. 5.

4.3.3 5 kHz third-octave band

Compared with the 2 kHz third-octave band, no sources can be found near the hub. This indicates that potential sound sources in this area are of lower source strength than in other mechanisms. As before, sound sources are located in the upper third of the fan blade, near the blade tip.

For $\Phi \in [0.065, 0.105]$, dominant sound sources due to flow separation are found near the leading edge and on the first half of the fan blade. For $\Phi \in [0.14, 0.18]$, the sources are distributed on the entire blade, hinting at noise generation due to the turbulent boundary layer. For $\Phi = 0.22$, sources can be found near both the leading and trailing edges, with sources near the trailing edge having higher sound power levels than the sources at the leading edge.

The former are caused by vortex shedding from the trailing edge (Wagner et al. 1996; Carolus 2013). The maximum sound power levels can be observed on the trailing edge with $L_p = 47$ dB for $\Phi = 0.22$ and the second highest with $L_p = 45.3$ dB on the blade leading edge for $\Phi = 0.065$. Thus, in this frequency range, significant sound sources can be found at different regions on the fan blade, depending on the flow rate coefficient.

4.3.4 8 kHz third-octave band

For $\Phi \in [0.065, 0.14]$, sound sources are located on the blade leading edge and on the hub. Multiple sources can be found near the hub at slightly greater radii, as in the 2 kHz third-octave band. This hints at noise generation due to small-scale turbulent structures, as generated by the flow over uneven surfaces, e.g., the transition area between fan hub and fan blades or between adjacent fan blades. Sources on the leading edge again indicate sound generation due to flow separation.

For higher flow rate coefficients $\Phi \in [0.18, 0.22]$, sound sources near the hub are negligible, as sources toward the blade tips become more dominant. Whereas at $\Phi \leq 0.14$ sound sources are mainly located on the leading edge, at $\Phi \geq 0.18$ sources occur on both the leading and trailing edges. Therefore, a transition from leading edge noise at low flow rate coefficients to trailing edge noise at high flow rate coefficients can be observed in the 8 kHz third-octave band.

4.3.5 Integrated spectra

For each fan blade, two different integration sectors are defined, corresponding to the respective leading and trailing edges. The calculated sound pressures in these sectors are summed and depicted as third-octave band spectra. The sectors and spectra are shown in Fig. 8. In general, lines of the same respective sectors are in close proximity, implying that the chosen algorithm yields comparable results for each fan blade.

At the lowest flow rate coefficient of $\Phi = 0.065$, sound from the leading edge sector is dominant over a frequency range $f \in [1.6$ kHz, 16 kHz$]$. This is in accordance with the sound maps in Fig. 7 for $\Phi = 0.065$. At this low flow rate coefficient, sound sources are mostly located in the leading edge area, as a result of flow separations due to the operation in the deep-stall region on the fan characteristic curve.

For frequencies below 1.6 kHz, the leading and trailing edge spectra are of similar magnitude, and for $f < 1$ kHz,
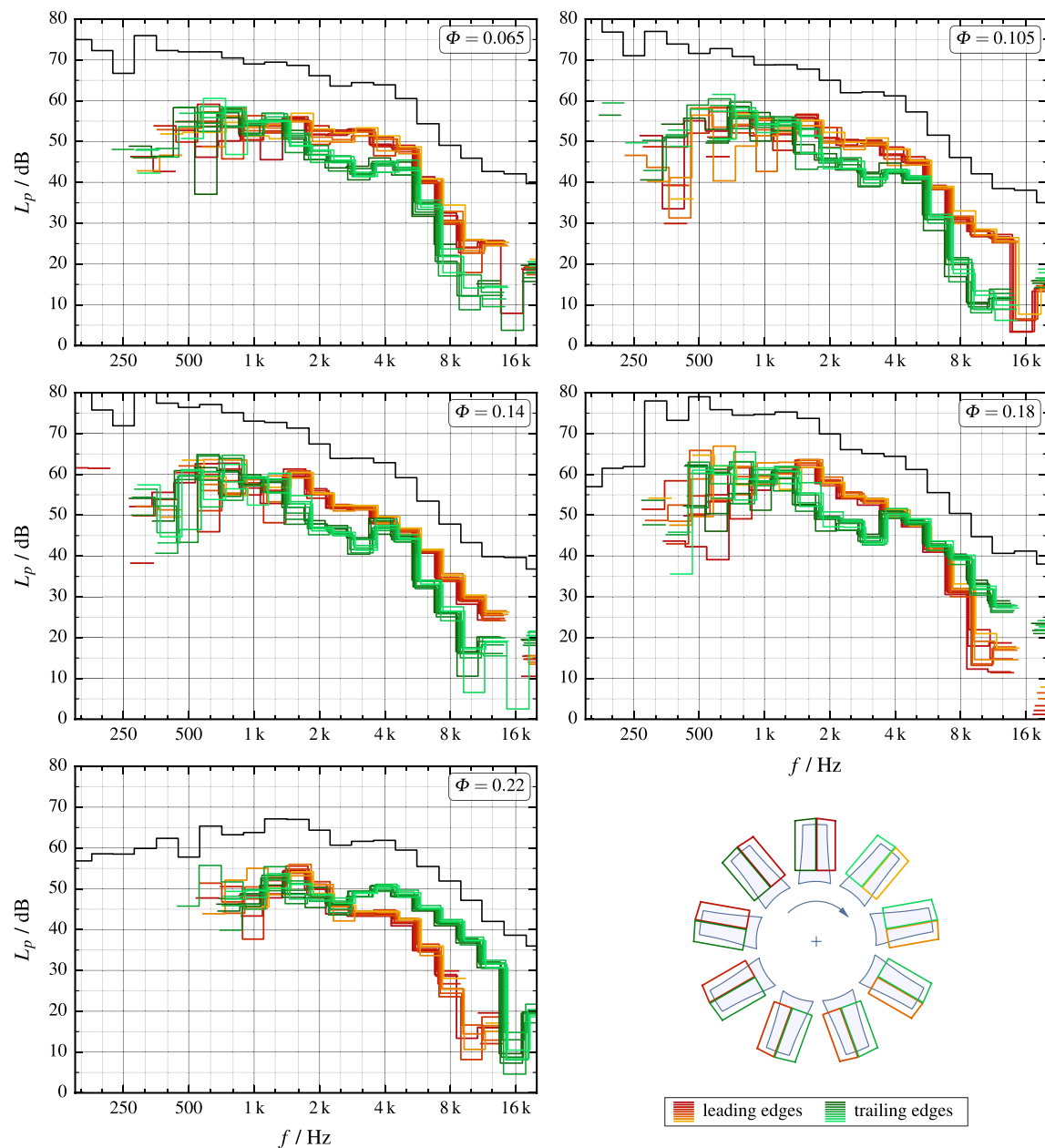
Fig. 8 Integrated spectra for different flow rate coefficients and integration sectors

the integrated levels deviate between similar sector types. This confirms the resolution limit for lower frequencies already mentioned in Sect. 4.3.

Similar observations can be made for a flow rate coefficient of $\Phi = 0.105$. Sound from the leading edges integration sector predominates for $f > 1.6\,\text{kHz}$. Sound from the trailing edges is again of equal magnitude for $f < 1.6\,\text{kHz}$.

At $\Phi = 0.14$, again sound from the leading edges integration sector is dominant for $f > 1.6\,\text{kHz}$. However, for frequencies around 4 and 5 kHz, the trailing edge spectra feature a local maximum, with an integrated sound pressure level of only 2 dB below that of the leading edges. As

shown in the previous section, sources in this frequency range mostly are distributed over the whole blade, hinting at noise generation due to the turbulent boundary layer.

So far, all considered operating points of $\Phi \in [0.065, 0.14]$ are in the stall region. Hence, inevitable flow separations occur at or near the blade leading edges. As a consequence, spectra from the leading edge integration sectors outvalue spectra from the trailing edge sectors.

At the design flow rate coefficient of $\Phi = 0.18$, the spectrum up to $f = 3.15\,\text{kHz}$ is dominated by sound from the leading edge sectors. At higher frequencies, levels from the trailing edge integration sectors are equal ($f \in [4, 6.3\,\text{kHz}]$)

or higher ($f > 6.3\,\text{kHz}$). This can also be observed in the sound maps (Fig. 7), where sound sources are located near the leading edge for low frequencies and then shift toward the trailing edge with increasing volumetric flow.

The change from leading to trailing edge noise can be observed at lower frequencies for $\Phi = 0.22$. Here, the levels from sound of the trailing edge integration sectors surpass the curve from the leading edge sectors already at $f = 2.5\,\text{kHz}$. As the blades are only moderately loaded at this operating point, noise generated on the leading edge or the blade surface becomes less significant and trailing edge noise predominates.

5 Summary

The microphone array method using the virtual rotating microphone array proved capable of resolving sound sources on the blades of a generic unskewed fan. Sound maps for third-octave bands with center frequencies between 1 and 8 kHz were presented. Furthermore, integrated spectra for leading and trailing edge integration sectors were discussed.

Both sound maps and integrated spectra provide indications of the underlying physical mechanisms of how and at what location sound is generated at various flow rate coefficients and frequency ranges. It can be stated that at very low flow rate coefficients, i.e., with a relatively low volumetric flow and high static pressure difference, sound from the fan blade leading edges is the most dominant mechanism. Sound in this region stems either from flow separations near the leading edges or from the interaction of the blade leading edges with the inflow.

For higher volumetric flows, sound sources shift toward the trailing edges, as vortex shedding here becomes the major noise-generating mechanism. This is most significant if the fan blades are only moderately loaded and the relative inflow velocity to the fan blades is high. Integrated spectra also show a shift from leading to trailing edge noise for higher volumetric flows, confirming the observations from the sound maps.

For the sound maps, the lowest evaluated frequency band was the 1 kHz third-octave band. It was found that no clear repetitive pattern, corresponding to the fan blades, could be resolved in this frequency range. Deviating levels of the integrated spectra at lower frequencies confirm the spatial resolution limits of the method.

This investigation showed that major noise-generating mechanisms are not limited to fan components emitting sound at specific frequencies, but rather that the main contributing mechanism depends strongly on the operating point. Therefore, approaches to the optimization, i.e., for the reduction in one particular sound mechanism, always necessitate prior knowledge of the fan's operating point in the particular installation environment.

References

Bamberger K, Carolus T (2012) Optimization of axial fans with highly swept blades with respect to losses and noise reduction. In: Proceedings of the international conference on fan noise, technology and numerical methods 2012, Senlis, France

Benedek T, Tóth P (2013) Beamforming measurements of an axial fan in an industrial environment. Period Polytech 57(2):37–46. doi:10.3311/PPme.7043

Benedek T, Vad J (2014) Concerted aerodynamic and acoustic diagnostic of an axial flow industrial fan, involving the phased array microphone technique. In: Proceedings of ASME Turbo Expo 2014

Blake WK (1986) Mechanics of flow-induced sound and vibration. Academic Press, Cambridge

Carolus T (2013) Ventilatoren-Aerodynamischer Entwurf, Schallvorhersage, Konstruktion, vol 3. Springer

Chou SR (1990) A study of rotor broad band noise mechanisms and helicopter tail rotor noise. NASA-CR 177565 National Aeronautics and Space Administration

Dougherty R, Ramachandran R, Raman G (2013) Deconvolution of sources in aeroacoustic images from phased microphone arrays using linear programming. Int J Aeroacoust 12(7–8):699–718. doi:10.1260/1475-472X.12.7-8.699

Dougherty RP, Walker BE (2009) Virtual rotating microphone imaging of broadband fan noise. AIAA Paper 2009-3121

Herold G, Sarradj E (2015) Microphone array method for the characterization of rotating sound sources in axial fans. Noise Control Eng J 63(6):546–551

Herold G, Sarradj E (2016) Frequency domain deconvolution for rotating sources on an axial fan. In: Berlin Beamforming Conference BeBeC 2016

ISO (2007) ISO 5801:2007 industrial fans—performance testing using standardized airways

Kim JH, Ovgor B, Cha KH, Joo-Hyung K, Lee S, Kim KY (2014) Optimization of the aerodynamic and acoustic performance of an axial-flow fan. AIAA J 52(9):2031–2044. doi:10.2514/1.1052754

Lowis CR, Joseph PF (2006) Determining the strength of rotating broadband sources in ducts by inverse methods. J Sound Vib 295:614–632. doi:10.1016/j.jsv.2006.01.031

Minck O, Binder N, Cherrier O, Lamotte L, Budinger V (2012) Fan noise analysis using a microphone array. In: Proceedings of the international conference on fan noise, technology and numerical methods 2012, Senlis, France

Pannert W, Maier C (2014) Rotating beamforming - motion-compensation in the frequency domain and applications of high-resolution beamforming algorithms. J Sound Vib 333:1899–1912

Sarradj E (2012) Three-dimensional acoustic source mapping with different beamforming steering vector formulations. Adv Acoust Vib 2012:1–12. doi:10.1155/2012/292695

Sijtsma P (2007) CLEAN based on spatial source coherence. Int J Aeroacoust 6(4):357–374. doi:10.1260/147547207783359459

Sijtsma P (2010) Using phased array beamforming to identify broadband noise sources in a turbofan engine. Int J Aeroacoust 9(3):357–374. doi:10.1260/1475-472X.9.3.357

Sijtsma P, Oerlemans S, Holthusen H (2001) Location of rotating sources by phased array measurements. AIAA Paper 2001-2167

Underbrink J (2002) Aeroacoustic phased array testing in low speed wind tunnels. In: Aeroacoustic measurements. Springer, Berlin, pp 98–215

Wagner S, Bareiß R, Guidati G (1996) Wind turbine noise. Springer, Berlin

Wright SE (1976) The acoustic spectrum of axial flow machines. J Sound Vib 45(2):165–223. doi:10.1016/0022-460X(76)90596-4

Zenger F, Becher M, Becker S (2015) Influence of inflow turbulence on aeroacoustic noise of low speed axial fans with skewed and unskewed blades. In: Proceedings of the international conference on fan noise, technology and numerical methods 2015, Lyon, France